Mechanical Properties of X3NiCoMoTi 18-9-5 Produced via Additive Manufacturing Technology – Numerical and Experimental Study

Robert Owsiński[1], Rafael Miozga[2], Agnieszka Łagoda[3], Marta Kurek[1*]

[1] Department of Mechanics and Machine Design, Faculty of Mechanical Engineering, Opole University of Technology, ul. Mikołajczyka 5, 46-020 Opole, Poland

[2] Science and Technology Park in Opole, ul. Technologiczna 2, 45-839 Opole, Poland

[3] Department of Manufacturing and Materials Engineering, Faculty of Mechanical Engineering, Opole University of Technology, ul. Mikołajczyka 5, 46-020 Opole, Poland

* Corresponding author's e-mail: ma.kurek@po.edu.pl

ABSTRACT

The purpose of the article was to analyze the influence of print orientation, using the direct metal laser sintering (DMLS) method, on the strength of the tested material before and after heat treatment. The heat treatment involved heating the material to 490 °C and subsequently cooling it within the furnace for four hours. Experimental research involves the X3NiCoMoTi 18-9-5 tool steel. Analysis of the test results indicates a strength increase following heat treatment. Additionally, a numerical study was conducted to investigate the mechanical characteristics of the X3Ni-CoMoTi 18-9-5 tool steel fabricated via 3D printing. Fractographic analysis of specimen failure was performed, and the results were subsequently compared.

Keywords: DMLS, maraging steel, strength analysis, numerical analysis, heat treatment, anisotropy, fracture analysis.

INTRODUCTION

In recent years, there has been a noticeable upward trend in the utilization of components fabricated through unconventional additive techniques based on metal powders in engineering structures, particularly in the aviation and medical sectors [1]. 3D printing involves the layer-by-layer application of material, each characterized by specific structure and thickness, resulting in a finished product that mirrors the digital model. The growing interest in such components mainly stems from the extensive adaptability to the operating conditions they offer. The opportunities presented by additive manufacturing technologies are often beyond the reach of conventional manufacturing methods due to such factors as high costs, intricate geometries, or specific parameters of the produced component. By selecting appropriate manufacturing parameters, such as laser power, sintering time, single-layer thickness, and growth direction, additive manufacturing enables manipulation of the final mechanical properties of the component. Moreover, it generates minimal waste and is energy-efficient [2]. Despite numerous advantages, it comes with drawbacks like the need for support removal and surface finishing to enhance quality. Notably, one of the significant concerns is the anisotropy within the structure of the material. Numerical studies are essential for understanding and mitigating these challenges.

Metal additive manufacturing (MAM), commonly referred to as metal three-dimensional (3D) printing, is a process that involves the joining of metallic materials (in powder, wire, sheet forms, etc.) to fabricate objects from 3D models, typically layer by layer [3]. MAM has the potential to revolutionize the design and construction of metallic items in the digital industrial era [4, 5]. The sales of metal AM systems have witnessed a significant surge in recent years. Correspondingly, there has been a noticeable increase

in research interest in metal AM, particularly in the last five years [6, 7], with the most significant surge in publications observed in 2019 [8].

In recent years, 3D components have become indispensable elements in numerous engineering sectors, particularly in medical and aerospace applications [9]. This is attributed to the ability to significantly alter mechanical characteristics during production by employing appropriate strategies for printing materials, such as printing parameters and element arrangement within the printer. Finished components can undergo post-processing similar to conventional elements, albeit at the expense of increased labor and manufacturing time. However, this process notably enhances surface quality and reduces the stair-stepping effect inherent in any additive manufacturing (AM) process [10, 11]. Variations in energy input can serve as a primary variable leading to diverse surface topographies and material porosity [12]. Presently, 3D printing presents a myriad of new possibilities, elevating production processes to unprecedented levels by enabling the direct printing of necessary elements or functional parts [13, 14]. Traditionally, Co-Cr-Mo alloys are fabricated using wrought and casting methods, but with advancements in 3D printing technology, biomedical implants and components can be rapidly manufactured from the same material. Of even greater importance is the ability to tailor individual parameters for each person, simultaneously offering reduced costs, shorter production times, and positive environmental impacts [15]. Moreover, research [16] demonstrates that the DMLS method surpasses the stir casting method due to lower dimensional errors. Printing from metal powder also has its disadvantages, the main ones are warping or cracking of the components as a result of residual stresses or thermal gradients, which directly impacts the final component structure. Components strength, durability or fatigue resistance may be reduced [17].

Wöhler's company specializing in technology analysis published a report showing that the global metal 3D printing industry generated revenue of almost $40 billion in 2023 [18]. The fundamental mechanical properties are typically determined through appropriate experiments conducted on the samples extracted from the test material. In most cases, neither the location nor the direction of sampling affects the mechanical properties of the sample. In such instances, the tested material is described as homogeneous and isotropic. However, the scenario differs for printed materials. This technology enables direct production of high-quality metal parts based on 3D CAD models, resulting in the samples characterized by anisotropic properties [19].

The anisotropy of materials significantly impacts their strength, both under static and fatigue conditions. Consequently, there has been a growing interest in recent years in analyzing the influence of structural directionality on material properties. Various materials undergo analysis, including aluminum alloys [20], where the rolling direction alters their properties to some extent [21], and composite materials, where the orientation of the fiber arrangement notably affects their parameters [22]. Additionally, there has been an increasing focus on the effect of structural anisotropy in elements produced via additive manufacturing on fatigue life.

The paper presents both numerical and experimental investigations conducted on the specimens produced via additive manufacturing, before and after heat treatment. Numerical studies are an increasingly valuable tool in engineering. The appropriate preparation of the test model can provide insight into both the static behavior and fatigue strength of materials, taking into account parameters such as the size and depth of the notches or the percentage and method of filling the element [23, 24]. The heat treatment process involved heating the material to 490 °C and subsequently cooling it within the furnace for four hours. The X3NiCoMoTi 18-9-5 tool steel was the material for testing. Furthermore, the analysis considered material anisotropy by implementing an appropriate specimen printing strategy. The heterogeneity arises from the influence of high temperatures and the layer-by-layer additive manufacturing technique.

The scientific innovation within this study lies in the utilization of non-standard numerical analyses, precisely integrating the parameters of the 3D printing process and their effects into finite element method (FEM) modelling during tensile tests. This pioneering approach facilitates a more realistic representation of material behavior under 3D printing conditions. Additionally, optical profilometry was used to investigate the metrological parameters of fatigue fractures based on the direction of material growth. This methodology offers detailed insights into the material's microstructure and durability concerning fatigue, significantly contributing to the understanding of the mechanical properties of materials fabricated via 3D printing. The results of the numerical analyses were

compared with those of the experimental tensile tests, showing the validation of the adopted numerical models adopted and enhancing comprehension of the correlation between theoretical predictions and the actual behavior of the material observed in laboratory tests. Ultimately, this comprehensive analysis represents a significant advancement in the study of the mechanical properties of materials produced using 3D printing technology.

MATERIALS AND METHODS

Direct metal laser sintering printing method

The direct metal laser sintering method is a technique utilized to apply metallic powders. It involves several steps, including preheating the printing chamber with inert gas, spreading a thin layer of metallic powder through a recoater, selectively melting the powder particles with a high-power laser, reducing the platform by the thickness of a single layer, and repeating the process until the object is fully built. Subsequently, the model is removed from the printing base platform, and surface finishing procedures are conducted by removing supports.

The DMLS printing method entails applying material layers to the element and hardening it in place by surfacing the print line. However, due to the varying temperatures and duration of application of subsequent layers, local stresses arise in the material, resulting in an inhomogeneous material structure. These inhomogeneities are layered, aligned with the direction of the print line layers, and can significantly influence the strength of an element due to anisotropy. Heat treatment of the finished element can be employed to alleviate this adverse effect. Anisotropy refers to the variation in the value of a particular parameter on the direction of measurement. When printed using elevated temperatures, the layered bonding of elements causes anisotropy in the printed components [25]. Laser sintering leads to the formation of layers, undulations, and heterogeneity between individual printing paths.

The specimens were printed on an EOSINT M280 printer, with their printing angles and arrangement on the board depicted in Figure 1.

The EOSINT M280 enables the direct manufacturing of high-quality metal components solely based on 3D models. The printer boasts a spacious building area of 250 × 250 × 325 mm and is equipped with a laser power of either 200 W or 400 W. It is compatible with a wide range of metal powders, including aluminum alloys, titanium alloys, and even maraging steel X3NiCo-MoTi 18-9-5 [26].

Material and specimens

Due to the presence of anisotropy in the material, tests were conducted on specimens printed at various angles. These specimens, prepared accordingly, were utilized in research aimed at
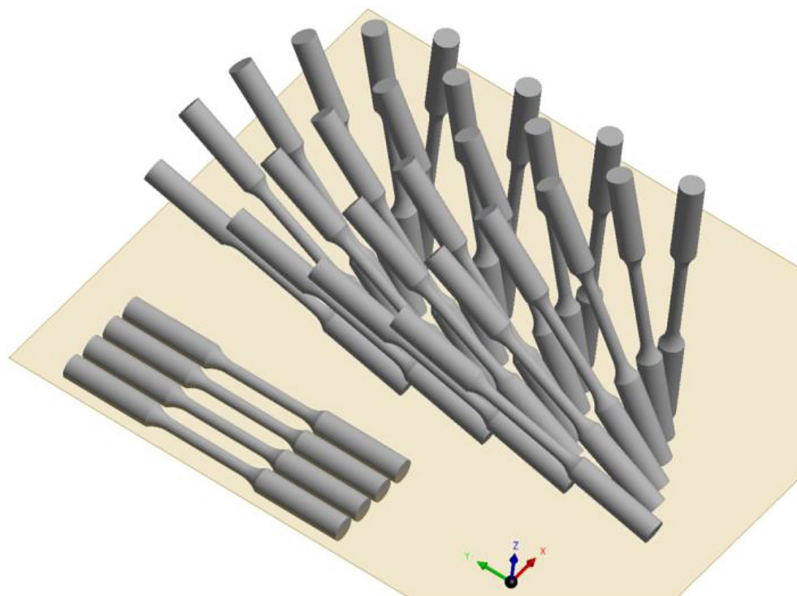
Figure 1. Specimens printing angles and board arrangement

determining whether the arrangement of the infill layers influences the strength of the tested material.

Round specimens (Figure 2) were intended for strength testing according to ISO 6892-1 standards. These specimens are fabricated from Maraging Steel MS1 powder. MS1 is also known under various classifications, including American designation 18 Maraging 300, European 1.2709, or German X3NiCoMoTi 18-9-5. The material is characterized by its high strength and toughness, commonly utilized in complex tooling, die casting molds, as well as engineering application parts and spare components [26]. Table 1 presents the static properties of the tested material immediately after printing, based on the manufacturer's data. Table 2 provides a summary of the chemical composition of this material. The printing strategy involved printing specimens at various angles: 0°, 15°, 30°, 45°, 60°, 75°, and 90° relative to the printing surface. Various angles of printed elements may impact their performance and fracture strength [28, 29]Some specimens from each series underwent thermal stress relief at 490 °C, followed by a four-hour cooling period in an oven. Utilizing this process facilitates localized hardening, thereby enhancing strength parameters such as yield strength and tensile strength.

The selection of heat treatment parameters for maraging steel, specifically heating the material to 490 °C and cooling it in an oven for four hours, is a meticulously calculated process integral to optimizing the mechanical properties of the material. The rationale behind the choice of 490 °C lies in the precipitation-hardening mechanism inherent to maraging steels. At this temperature, the alloying elements within the steel, typically nickel, cobalt, and molybdenum, undergo controlled precipitation, forming intermetallic compounds that significantly contribute to the material strength and hardness.

Deviation from the specified temperature could have profound effects on the microstructure and, consequently, the mechanical characteristics of the steel. A lower temperature might hinder the desired precipitation reactions, resulting in insufficient strengthening. Conversely, a higher temperature could lead to the formation of coarse precipitates, potentially inducing brittleness and compromising the material toughness. The four-hour cooling duration in the oven is designed to ensure a gradual and controlled cooling rate, allowing adequate time for the precipitation process to occur. An abbreviated cooling period might not provide sufficient time for the alloying elements to form the desired precipitates effectively. On the other hand, an excessively prolonged cooling time might lead to over-aging, causing a decline in toughness and impact resistance.

In the realm of maraging steel research and metallurgical practices, the specific heat treatment parameters — heating to 490 °C and subsequent four-hour cooling — are well-documented and actively explored by researchers and practitioners in
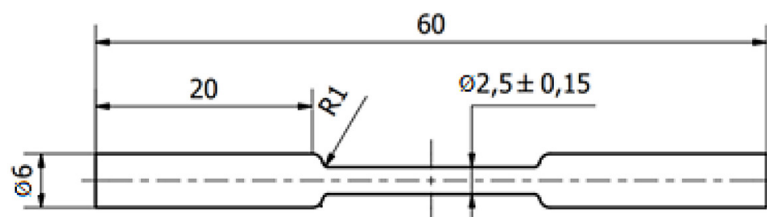

Figure 2. Geometry of round specimens used for strength tests

Table 1. Static properties of the X3NiCoMoTi 18-9-5 steel

Properties	R_m [MPa]	$R_{0,2}$ [MPa]	A_5 [%]
Before the heat treatment	1200	1020	13
After the heat treatment	2060	1990	4

Table 2. Chemical composition of the X3NiCoMoTi 18-9-5 steel in % [27]

C	Si	Mn	Mo	Ni	Co	Ti	Fe
0.03	0.10	0.15	4.90	18.00	9.30	1.10	balance

the field. In the results reported by Mutua et al. and Bai et al. [30, 31], these parameters have been a focal point of investigation, reflecting a shared interest in understanding and optimizing the mechanical properties of maraging steel. This precision in temperature and time parameters is fundamental in tailoring the material properties of maraging steel to meet specific performance requirements.

The tests were conducted using an Instron ElectroPlus E10000 fatigue testing machine. This electric test instrument is designed for dynamic and static testing on a wide range of materials and is capable of performing at frequencies exceeding 100 Hz [32]. Figure 3a and Figure 3b display metallographic images of two selected specimens printed at angles of 0° and 30°, respectively. The fracture spot is not noticeable due to the specimen size and the resolution of the image. Analysis of the fractured images reveals that the fractures occurred along the print lines, corresponding to the angles at which the specimens were printed. The crack pattern along the print lines indicates the anisotropy of materials printed using the DLMS method.

## Numerical approach – exporting nodal data

The analysis of 3D printing processes often necessitates acquiring crucial information regarding stress and strain distributions within the analyzed component. Ansys offers a variety of tools and functionalities, including the APDL (ansys parametric design language) commands, to accomplish this task. These commands enable researchers to extract specific data from the analysis, providing valuable insights into the behavior of the printed part.

One set of commands commonly utilized in 3D printing analyses is UVECTORS. UVECTORS represent displacement vectors in the finite element model, enabling researchers to ascertain changes in node positions resulting from loading and deformation. By comparing the initial node positions with their displacements, linear deformations can be calculated, assisting in establishing stress distributions within the analyzed component.

In addition to UVECTORS, other essential sets of results can be obtained by utilizing APDL commands, such as EPELVECTORS, EPPLVECTORS, and EPPLEQV_RST. EPELVECTORS represent element plastic strain vectors, providing valuable information about the plastic deformation occurring within the finite elements. EPPLVECTORS, on the other hand, represent element plastic strain rate vectors, enabling the analysis of the dynamic behavior of plastic deformations during the 3D printing process. Lastly, EPPLEQV_RST indicates the plastic strain rate of an element, offering insights into the current behavior of the material regarding plastic deformations.

These result sets, obtained through the APDL commands, can be further enhanced by incorporating user-defined results (Figure 4). User-defined results enable researchers to extract specific data
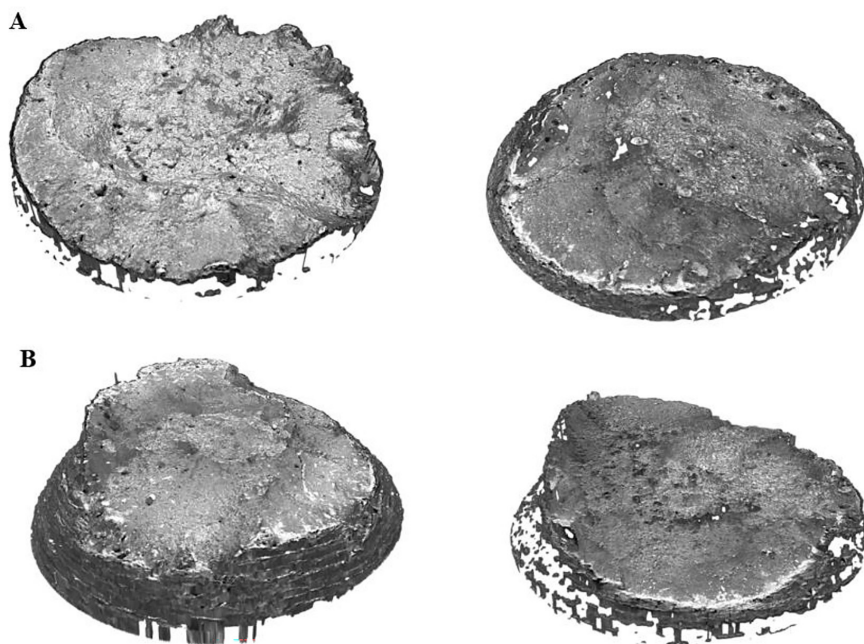
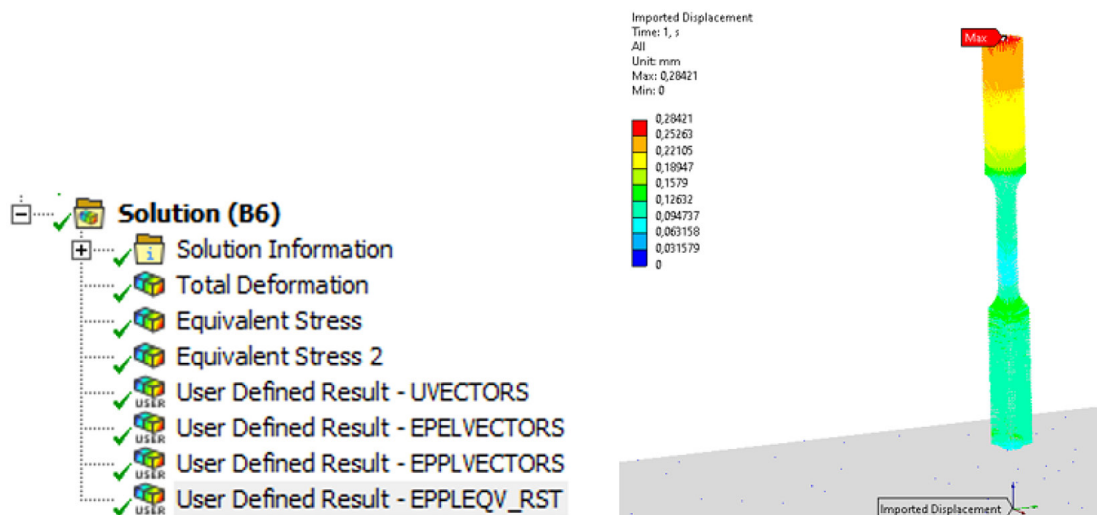**Figure 3.** Fracture of specimens printed at a – 0° and b – 30° angle

Figure 4. Exported information from AM analysis and summary imported loads (new system)

of interest tailored to their analysis requirements. By combining these user-defined results with the APDL commands, a comprehensive set of information about stress, strain, and plastic deformation characteristics can be obtained.

However, the acquired results are not limited to their usage within the initial analysis. To fully capitalize on the obtained data, the results must be imported into a new, independent analysis module using the External Data functionality provided by Ansys. This process ensures seamless integration of the acquired UVECTORS, EPELVECTORS, EPPLVECTORS, and EPPLEQV_RST data into the subsequent analysis. By incorporating these result sets into the new module, researchers can establish a steady-state condition for the 3D-printed component after printing.

RESULTS

Experimental data

As part of the study, a tensile test was conducted, involving the axial tension of the specimens, allowing for the continuous increase of force from zero to the value at which the specimen fractures. The research was conducted at ambient temperature for both pre- and post-heat treatment specimens.

The results of the static tensile test for round specimens made of the X3NiCoMoTi 18-9-5 steel before heat treatment are presented in Table 3, while the results for specimens after heat treatment are presented in Table 4. Upon

analyzing the data presented in Table 3, slight variations in tensile strength can be observed depending on the layer overlap angle of the printed samples. Tension diagrams generated from the obtained results allow for the interpretation of tensile force and other strength properties of the material. It is noteworthy that the results depicted in the charts align, providing evidence of the research reliability.

Furthermore, an analysis of the results presented in Table 4 reveals that the tensile strength of the samples after undergoing the heat treatment process is up to 70% higher than that of untreated samples. Additionally, these treated samples exhibit deformation, indicating higher plasticity. However, the tested strength parameters are several percent lower than those provided by the manufacturer. Figure 5a-g depicts tensile diagrams for round samples printed at various angles to the printing plane, both before and after undergoing heat treatment.

Numerical research

In this study, a comprehensive approach involving the exportation of nodal data from a thermomechanical coupled analysis using Ansys' External Data functionality (Figure 6) was presented. The exported data, comprising EPL (equivalent plastic strain), EPPL (equivalent plastic strain rate), EPPLRST (equivalent plastic strain at reset), and UVECTORS (displacement vectors), were employed in an independent analysis module. The primary objective of this module is to establish the steady-state condition

Table 3. Strength parameters for Maraging Steel MS1 before heat treatment

| Specimen number	Diameter [mm]	Young's modulus [GPa]	Yield strength 0.2% [MPa]	Strain for plasticity boundary [%]	Max. force [kN]	Tensile strength [MPa]
0°_S1_bHT	2.51	172.87	1116	0.84	5.92	1196
0°_S2_bHT	2.49	182.76	1109	0.81	5.89	1210
0°_S3_bHT	2.51	172.98	1089	0.75	5.99	1210
15°_S4_bHT	2.50	177.77	1010	0.76	6.00	1221
15°_S5_bHT	2.50	180.94	1052	0.78	5.87	1197
15°_S6_bHT	2.49	179.31	1125	0.82	5.93	1218
30°_S7_bHT	2.50	182.61	949	0.71	5.78	1177
30°_S8_bHT	2.49	190.56	1008	0.73	5.86	1204
30°_S9_bHT	2.50	193.60	972	0.70	5.86	1193
45°_S10_bHT	2.50	176.48	902	0.71	5.36	1093
45°_S11_bHT	2.50	168.52	894	0.72	5.28	1075
45°_S12_bHT	2.50	172.56	899	0.71	5.31	1081
60°_S13_bHT	2.50	170.87	1066	0.82	5.93	1208
60°_S14_bHT	2.50	168.76	1059	0.82	5.87	1197
60°_S15_bHT	2.50	179.24	1064	0.80	5.89	1200
75°_S16_bHT	2.50	183.38	923	0.70	5.35	1090
75°_S17_bHT	2.50	179.51	916	0.71	5.36	1093
75°_S18_bHT	2.50	165.88	948	0.77	5.32	1084
90°_S19_bHT	2.50	187.80	932	0.70	5.31	1082
90°_S20_bHT	2.50	173.13	918	0.73	5.31	1081
90°_S21_bHT	2.50	187.80	988	0.70	5.37	1095

Table 4. Strength parameters for Maraging Steel MS1 after heat treatment

Specimen number	Diameter [mm]	Young's modulus [GPa]	Yield strength 0.2% [MPa]	Strain for plasticity boundary [%]	Max. force [kN]	Tensile strength [MPa]
0°_S22_aHT	2.51	182.81	1988	1.28	9.93	2007
0°_S23_aHT	2.50	185.12	1926	1.24	9.76	1988
0°_S24_aHT	2.50	176.40	1912	1.28	9.74	1985
15°_S25_aHT	2.51	189.38	1963	1.24	9.80	1981
15°_S26_aHT	2.51	179.47	-	-	9.42	1905
15°_S27_aHT	2.51	169.76	1698	1.20	8.64	1745
30°_S28_aHT	2.51	190.11	1901	1.20	9.42	1903
30°_S29_aHT	2.51	189.70	1848	1.17	9.56	1931
30°_S30_aHT	2.50	185.15	1814	1.18	9.36	1905
45°_S31_aHT	2.50	195.42	1864	1.15	9.48	1972
45°_S32_aHT	2.50	187.11	1903	1.21	9.76	1989
45°_S33_aHT	2.50	190.08	1963	1.23	9.72	1981
60°_S34_aHT	2.49	181.14	1938	1.26	9.82	2017
60°_S35_aHT	2.49	185.70	1838	1.18	9.37	1923
60°_S36_aHT	2.49	188.57	1892	1.20	9.58	1967
75°_S37_aHT	2.50	183.48	1873	1.22	9.58	1951
75°_S38_aHT	2.51	182.29	1925	1.25	9.90	2000
75°_S39_aHT	2.50	206.83	1873	0.96	9.70	1976
90°_S40_aHT	2.50	184.05	1923	1.24	9.84	2003
90°_S41_aHT	2.50	183.00	1991	1.22	9.66	1967
90°_S42_aHT	2.50	181.41	1836	1.21	9.43	1920
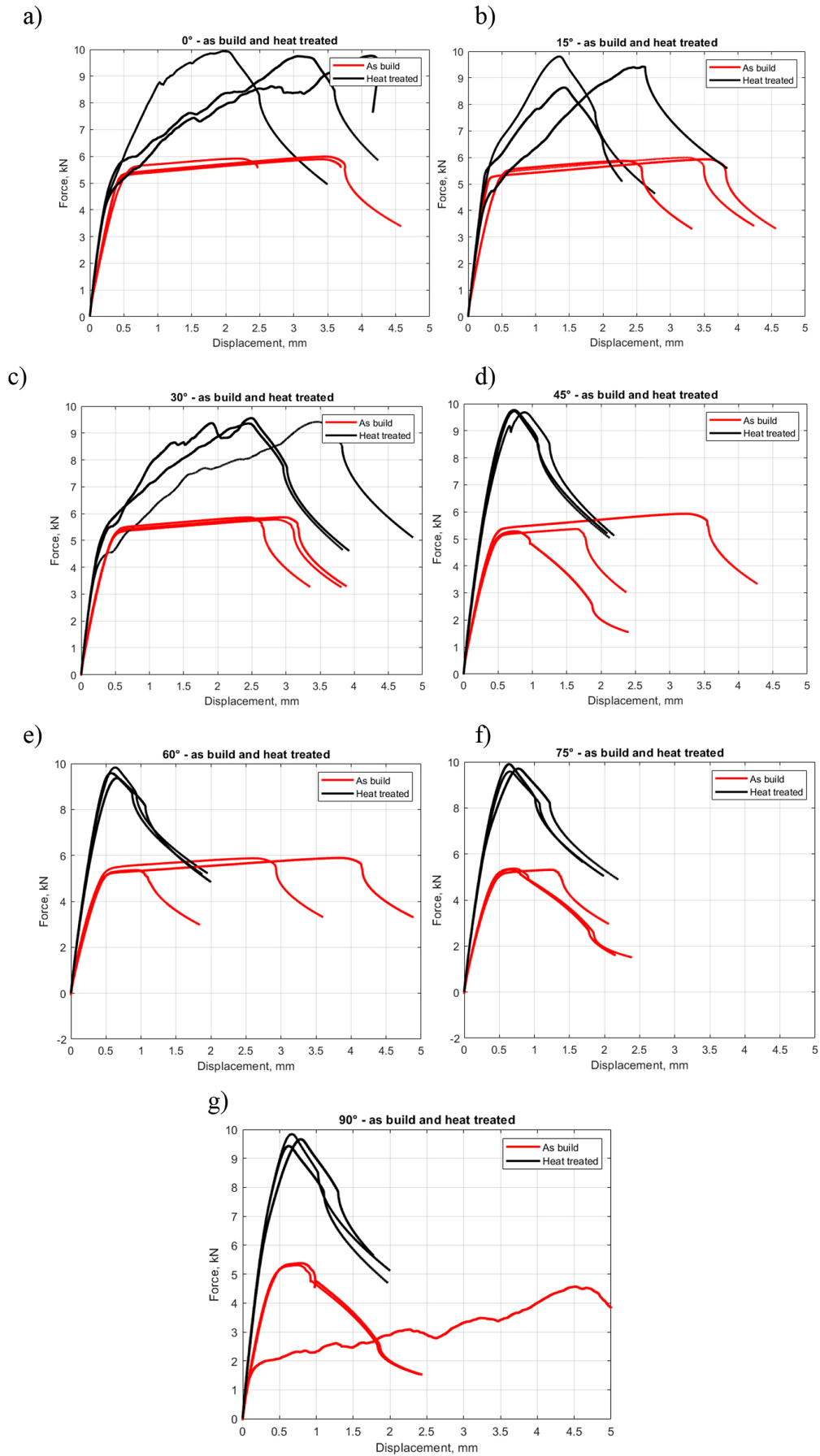
Figure 5. Tensile diagram for specimens before and after heat treatment printed with angles:
(a) 0°, (b) 15°, (c) 30°, (d) 45°, (e) 60°, (f) 75° and (g) 90°
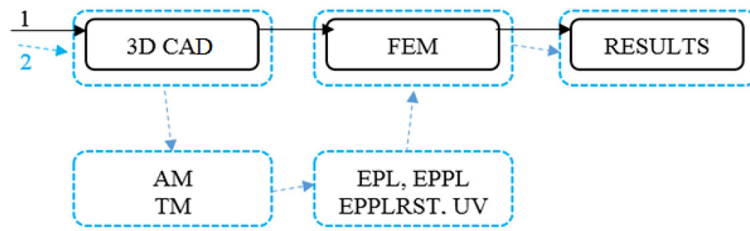
Figure 6. Comprehensive analysis using Ansys' External Data, where: 1 – regular approach to FEM analysis, 2 – FEM analysis approach that considers the printing conditions

of a 3D-printed component model subjected to a tensile test, which means the condition in the finite element modeling of the tensile test where the sample is considered after the 3D printing process, accounting for all effects resulting from the thermomechanical loads during the printing process, such as residual stresses in the sample. By integrating the nodal data from the thermomechanical analysis into the independent module, valuable insights into the mechanical behavior of the component after the 3D printing process can be gained.

To accurately model the stress distribution in a component manufactured using the 3D printing process with MS1 steel, the initial step is to create a precise 3D model of the component. This process is critical for obtaining reliable and precise results in numerical simulations. When preparing the 3D model, it is crucial to meticulously replicate the geometry and design specifics of the component manufactured with MS1 steel via 3D printing. Advanced CAD software like Autodesk Inventor is employed for precisely

modeling the component geometry. Proper integration of design elements such as supports, holes, and contact surfaces is imperative for accurately modeling the material behavior during the tensile test (Figure 7).

Accurately replicating the geometry and design details of the component holds significant importance for several reasons validating its validity. Firstly, a precise 3D model enables the accurate consideration of boundary conditions during simulation. By precisely representing the shape and specifics of the component, it becomes possible to apply appropriate forces or displacements necessary for reliable numerical analysis. Without an accurate 3D model, replicating real conditions of the tensile test would not be feasible. Secondly, a precise 3D model facilitates the generation of an accurate finite element mesh.

The analysis begins with simulating the heat transfer process, where the temperature distribution within the component and its surrounding environment is calculated. This step is crucial in capturing the thermal history of the material
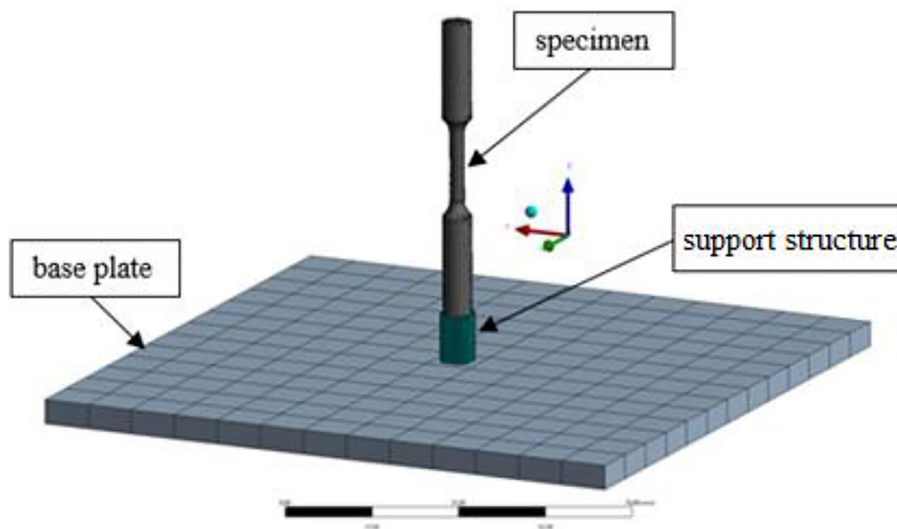
Figure 7. 3D specimen model with all necessary additional elements

throughout the 3D printing process. By accurately modeling heat transfer phenomena, temperature gradients and thermal stresses that develop within the component can be evaluated. Following this, mechanical loading is applied to the model to simulate the behavior of the printed component under external forces or constraints. This involves applying tensile forces to the component, depending on the specific analysis objectives. The mechanical analysis incorporates thermal effects identified in the previous step, as the response of the material is influenced by its temperature distribution. This constitutes a coupled thermomechanical analysis simulating the 3D printing process with the incremental addition of material layers and subsequent cooling to room temperature. The model, which includes the effects of the additive manufacturing process, was then used to simulate the tensile test by exporting the nodal data of the model. This process is graphically represented in Figure 6. The simulation outcomes furnish comprehensive information regarding various mechanical
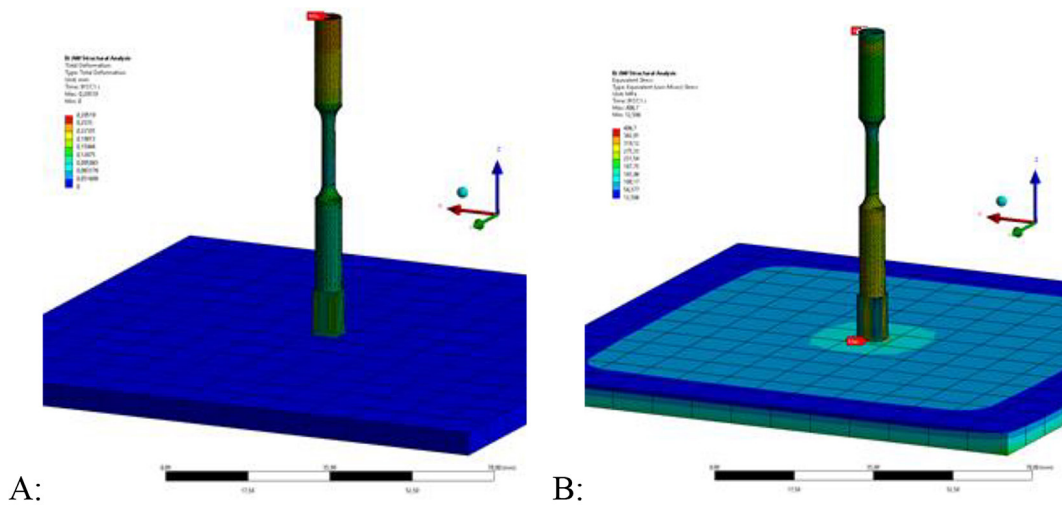

Figure 8. Displacement (a) and stress (equivalent) distribution (b) after AM process
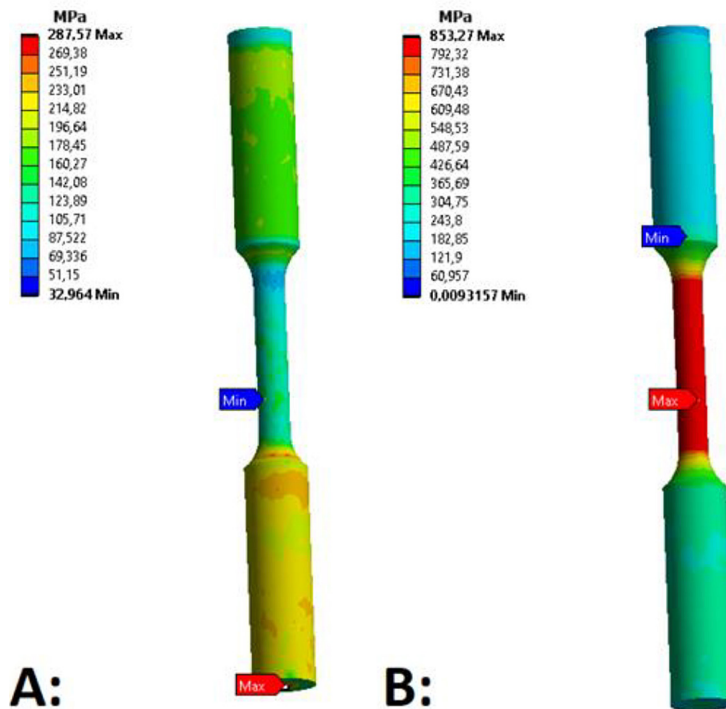

Figure 9. Residual stresses after AM process (a), results of static tensile test with 2.5 mm elongation (b) in MPa unit

parameters, encompassing displacement, stress (Figure 8a and Figure 8b), strain, and deformation. These results facilitate an evaluation of the structural integrity of the printed component and the identification of areas susceptible to failure or deformation. Through analysis of stress distribution, critical regions prone to excessive loading or potential material failure can be discerned.

The imported results can be leveraged to simulate and analyze the behavior of the printed part under diverse loading conditions. This integration augments researchers' comprehension of the mechanical properties, deformation characteristics, and stress distribution within the component (Figure 9a and Figure 9b). Consequently, it facilitates the optimization of the design and performance of the 3D-printed part for real-world applications. The results in Figure 9 were imported from the mechanical loading analysis of the finite element model that incorporates the thermal history from the 3D printing process.

Fracture analysis

Surface quality and roughness play pivotal roles in numerous engineering and manufacturing applications. Grasping the impact of production angles on surface roughness is paramount for process optimization and attaining desired product outcomes. This study sought to compare the surface roughness parameters of fracture samples manufactured at various angles and further the analysis by incorporating fractal parameters. Figure 10 illustrates the surface quality of selected specimens prior to heat treatment. Changes in parameters dependent on the production angle presented in Figure 11. Optical profilometry fracture analysis showed several dependencies:

- maximum peak height parameter (Sp) for 30°_S7_bHT (1533 μm) is higher than for 0°_S1_bHT (330 μm). Producing the sample at a 30° angle may result in increased surface roughness.
- waviness height (Sv) for 30°_S7_bHT (1196 μm) is greater than for 0°_S1_bHT (487 μm). Producing at a 30° angle can generate larger height variations on the surface.
- maximum height (Sz) for 30°_S7_bHT (2729 μm) is higher than for 0°_S1_bHT (818 μm). Producing at a 30° angle can introduce larger convexities on the surface.
- average roughness (Sa) for 30°_S7_bHT (486 μm) is greater than for 0°_S1_bHT (98 μm). Producing at a 30˚ angle can lead to an increase in the average height of peaks and valleys.
- skewness (Ssk) for 30°_S7_bHT (0.488) is positive, while for 0°_S1_bHT (-0.318), it is negative. Producing at a 30° angle can alter the asymmetry of the surface profile.
- kurtosis (Sku) for 30°_S7_bHT (2.276) is lower than for 0°_S1_bHT (3.379). Producing at a 30˚ angle may result in smaller extreme height values on the surface.
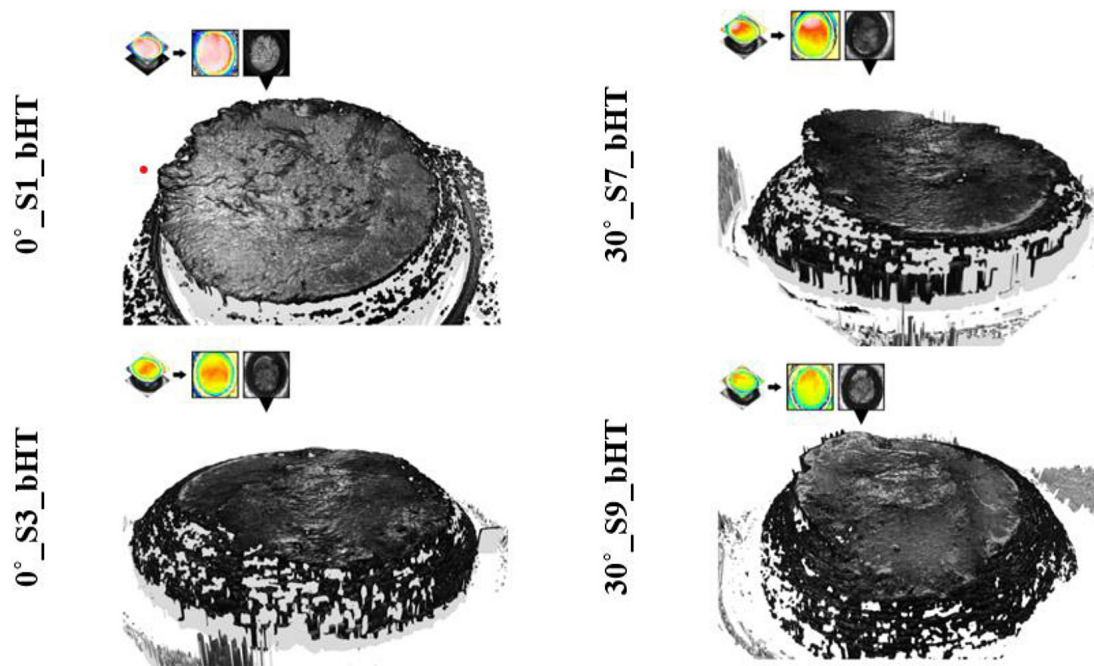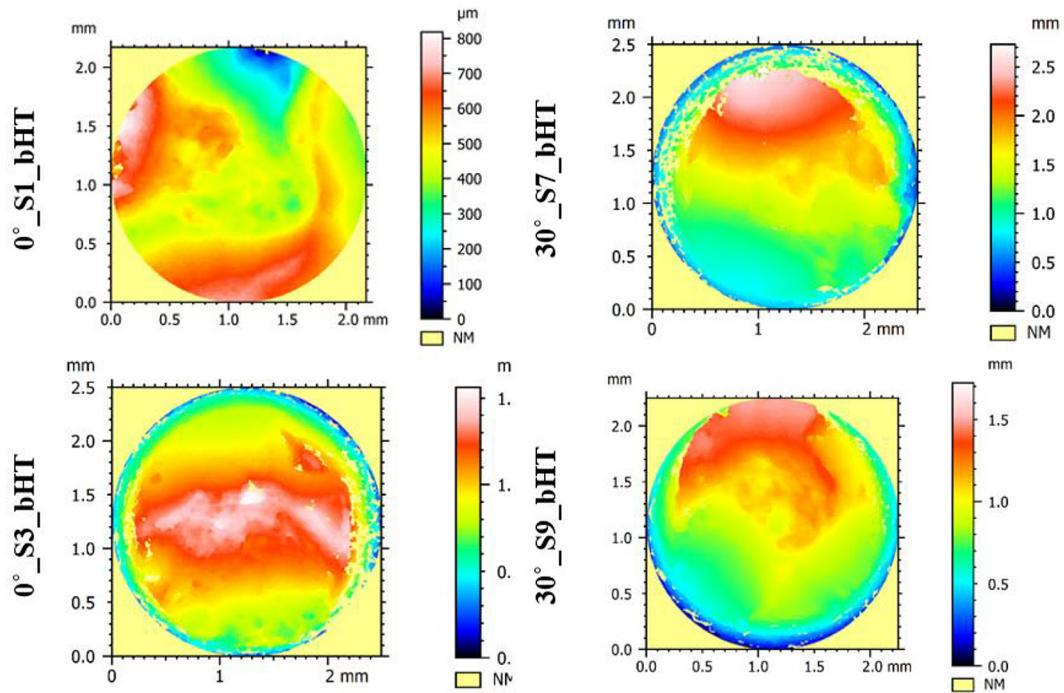

Figure 10. Surface quality of specimens with 0° and 30° printed angle

Figure 11. Changes in parameters of specimens printed at 0° and 30° angles using optical profilometry for fracture analysis

Table 5. Fractal results using SSFA

| Parameters	0°_S1_bHT	0°_S3_bHT	30°_S7_bHT	30°_S9_bHT
Smooth-rough crossover	345822 μm^2	638112 μm^2	943909 μm^2	558936 μm^2
Regression coefficient	0.9931	0.9843	0.9968	0.9923
Fractal complexity	24.95	37.93	31.48	44.36
Fractal dimension	2.050	2.076	2.063	2.089
The scale of max. complexity	9758 μm^2	4449 μm^2	522.9 μm^2	3567 mm^2

Fractal parameters obtained by scale-sensitive fractal analysis (SSFA) are presented in Table 5.

DISCUSSION

The experimental results closely aligned with the information provided by the MS1 powder producer. Prior to heat treatment, the mean tensile strength was 1152.62 MPa, which closely matched the producer's specification of 1200 MPa. Notably, the results for specimens printed at a 60° angle were particularly similar, with a mean value of 1201.97 MPa across three specimens. The research indicated that printing orientation significantly influenced specimen strength, with the specimens printed at a 15° angle exhibiting the highest mean tensile strength (1212 MPa), while those printed at a 45° angle demonstrated the lowest (1083 MPa). The mean value for plasticity boundary at 0.2% displacement (997.1 MPa) slightly deviated from the producer's specification (1020 MPa). Specifically, specimens printed at a 0° angle exhibited the highest mean value (1104.67 MPa), whereas those printed at a 45° angle showed the lowest (898.33 MPa).

The results after heat treatment also showed promising outcomes. The producer's specified tensile strength (Rm) was 2060 MPa, closely matched by the experimental mean value of 1953.14 MPa. Similarly, the producer's specified yield strength (R0.2) was 1990 MPa, with the experimental mean value at 1893.45 MPa, differing by less than 100 MPa. Notably, printing at a 0° angle orientation yielded the highest mean values for Rm (1993.33 MPa). However, it is worth mentioning that printing at a 0° angle orientation poses challenges due to the increased
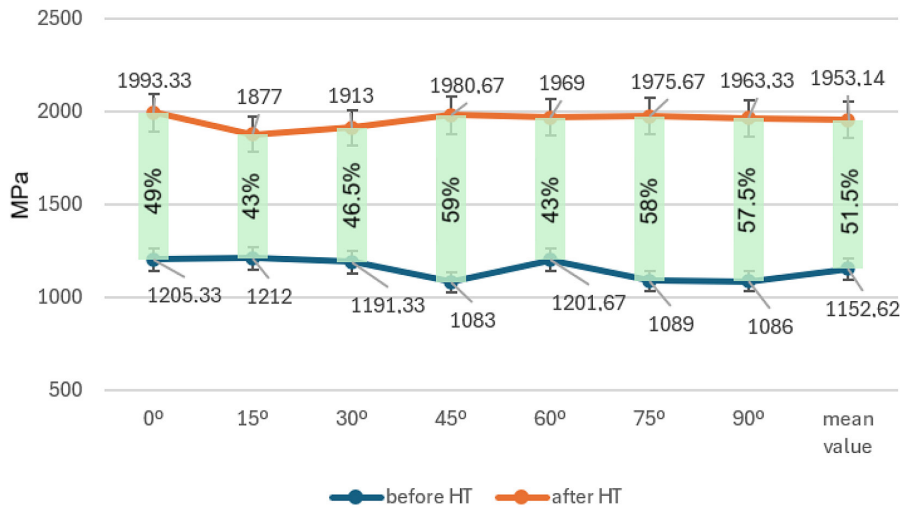
Figure 12. Comparison of experimental mean results value for every 3D printing orientation before and after treatment

requirement for printed supports. Figure 12 compares experimental mean values for every printed orientation before and after heat treatment and the percentage differences between the mean values. In general, the tensile strength after heat treatment is about 70% higher than the result before heat treatment.

The Young's Modulus remains consistent for specimens both before and after heat treatment, with a mean value of approximately 180 GPa
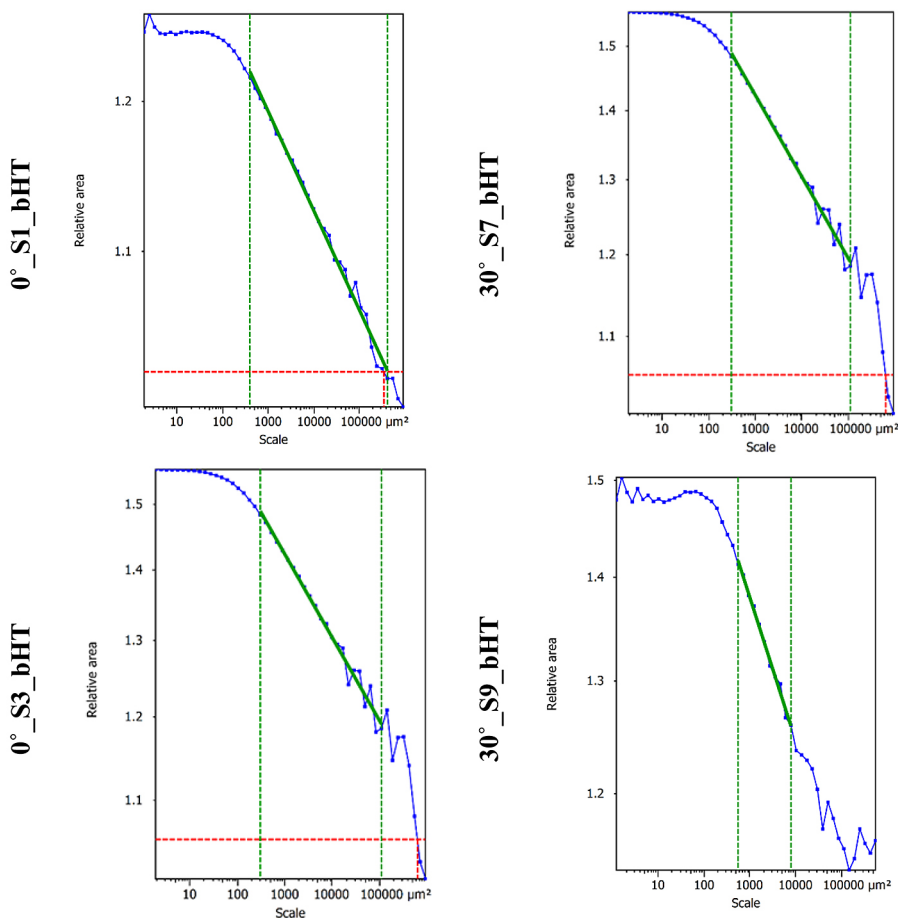
Figure 13. Relative areas for selected specimens obtained using optical profilometry surface quality analysis

in both cases. Moreover, this parameter exhibits similarity across all printing angles, indicating a consistent relationship between stress and strain for MS1 material regardless of heat treatment or printing angle.

Numerical research indicated a maximum tensile strength of 853.27 MPa (Figure 9b), whereas experimental research yielded a mean value of 1086 MPa. This discrepancy suggests the potential for further optimization in the printing process to achieve desired mechanical properties.

The optical profilometry surface quality analysis revealed that the production angle of specimens (0° vs. 30°) influences several surface roughness parameters, including the main parameter coefficient (Sp), waviness height (Sv), maximum height (Sz), average roughness (Sa), and kurtosis (Sku). These differences stem from variations in surface geometry, which can impact surface quality and properties across different applications. Figue 13 illustrates the relative area for selected specimens, highlighting these differences. The relative area in Figure 13 is defined as the ratio of the cross-sectional area at a given strain to the original cross-sectional area. This definition has been added to the figure caption for clarity.

On the basis of the results of the fractal analysis of the samples 0°_S1_bHT, 0°_S3_bHT, 30°_S7_bHT, and 30°_S9_bHT surface, the following sentences are noticeable:

- smooth-rough crossover (SRC): The SRC parameter helps identify the point at which more irregular elements appear on the surface. It is determined by analyzing the scale at which the surface roughness transitions from smooth to rough. It is typically computed by examining the change in the roughness parameter over different scales:

$$SRC = Area_{crossover} \qquad (1)$$

where: $Area_{crossover}$ is the area at which the roughness of the surface starts to increase significantly. For samples 0°_S1_bHT and 0°_S3_bHT printed vertically (0°), the SRC for 0°_S3_bHT (638112 μm^2) is notably higher than for 0°_S1_bHT (345822 μm^2), indicating that the surface of 0°_S3_bHT becomes more irregular on a larger scale. Conversely, for samples 30°_S7_bHT and 30°_S9_bHT printed at a 30° angle, the difference in SRC is less pronounced, suggesting that the printing angle may have a smaller impact on the transition point from a smooth to rough surface.

- regression coefficient R²: The R² value indicates the precision of complexity measurements. It is calculated to determine the goodness of fit for the fractal dimension measurements:

$$R^2 = 1 - \left(\frac{\Sigma(y_i - \hat{y}_i)^2}{\Sigma(y_i - \bar{y})^2} \right) \qquad (2)$$

where: y_i is the observed data, $\hat{y}_i$ is the predicted data from the model, and $\bar{y}$ is the mean of the observed data. All samples exhibit high R² values (above 0.98), indicating the accuracy of fractal measurements for all samples.

- fractal complexity (Asfc): The Asfc parameter measures the fractal complexity of the surface. It is a measure of how the complexity of the surface structure changes with scale:

$$Asfc = \frac{1}{A} \Sigma A_i \qquad (3)$$

where: A_i is the area of the surface at scale i, and A is the total area. *Asfc* values for samples 0°_S1_bHT and 30°_S7_bHT are similar (24.95 and 31.48, respectively), suggesting some similarity in complexity structure. However, samples 0°_S3_bHT and 30°_S9_bHT differ significantly in this regard (37.93 and 44.36, respectively), indicating that the printing angle may influence the fractal complexity of the surface.

- fractal dimension (Das): The Das parameter measures the fractal dimension of the surface. It quantifies the complexity of the surface by describing how detail in the surface changes with the scale of measurement:

$$Das = \lim_{\epsilon \to 0} \frac{\log N(\epsilon)}{\log\left(\frac{1}{\epsilon}\right)} \qquad (4)$$

where: $N_{(\epsilon)}$ is the number of self-similar structures at scale ϵ. Das values are similar for every selected sample, indicating some similarity in fractal dimension across all samples.

- scale of maximum complexity (Smfc): The Smfc parameter determines the scale at which the surface achieves its highest complexity. It indicates the scale at which the surface exhibits the highest fractal complexity:

$$Smfc = arg\,max(i)\left(\frac{d(Asfc)}{d(Scale_i)} \right) \qquad (5)$$

where: $Scale_i$ is the scale at which the complexity measure *Asfc* reaches its peak. For every tested sample, the differences in Smfc are relatively small, suggesting some similarity in this aspect.

CONCLUSIONS

After conducting analysis and research, several conclusions can be drawn. The orientation of printed component layers significantly influences material strength and stress distribution in the material. Also, the hardness and plasticity of the material may vary depending on the print orientation, which is the result of microstructural differences created during the layering process. Different orientations require different amounts of support material, which affects printing time and costs and the difficulty of removing supports after the process is complete.

Although the strength parameters slightly deviate from those provided by the MS1 powder producer, the results are largely consistent. Durability test results continue to be as expected, meaning that the material meets most of the technical specifications and expectations for its mechanical properties. Small differences can result from various factors, such as printing conditions, heat treatment, or the specificity of individual powder batches. Overall, MS1 samples perform to quality standards and exhibit consistent and predictable mechanical properties, making them suitable for their intended engineering and industrial applications.

The specimens subjected to heat treatment exhibit a tensile strength up to 70% higher than those without heat treatment. Heat treatment is a key post-processing stage that significantly affects the properties and quality of the final elements printed with 3D metal printing technology, adapting them to the requirements of various industrial applications. Heat treatment helps reduce stresses, which prevents deformation and cracking. Additionally, heat treatment can recrystallize the material, eliminating the columnar microstructure formed during printing and creating a more uniform microstructure with finer grains.

Maraging alloys, such as MS1, are designed to achieve high strength and hardness after heat treatment. A characteristic feature of these alloys is their ability to maintain a constant stress-strain relationship, which means that the elastic modulus of the material remains unchanged even after various heat treatment cycles (Table 3 and 4). In the case of maraging steel, heat treatment also aims to precipitate fine reinforcing phases in the martensite matrix, which improves mechanical properties without affecting the basic stress-strain relationship. Owing to this, even after hardening and aging processes, the material retains its elastic properties. Elongation of the specimens after heat treatment is different to those without heat treatment. After heat treatment of the MS1 material, a significant increase in its plasticity is observed increasing the value of tensile strength. Heat treatment leads to homogenization of the microstructure and removal of internal stresses, which translates into better mechanical properties; however, the elongation values indicate an increase in the brittleness of the material.

Fractal analysis reveals differences in complexity and surface structure between samples printed vertically (0°) and at a 30° angle. However, these differences are not drastic, indicating some similarities between these two groups of samples. The results highlight significant variations in surface roughness parameters among samples produced at different angles. Particularly, specimens with a 0° printing angle display smoother surfaces characterized by smaller peak-to-valley height differences and negatively skewed height distributions. Conversely, the 30° printing angle exhibits rougher surfaces with larger peak-to-valley height differences and positively skewed height distributions.

These differences in roughness can be attributed to the production angle and its influence on the printing process, material properties, and surface structure.

REFERENCES

1. Javaid M., Haleem A., Singh R.P., Suman R. 3D printing applications for healthcare research and development. Global Health Journal 2022; 6: 217–26. https://doi.org/10.1016/j.glohj.2022.11.001

2. Zhang M., Sun C.-N., Zhang X., Goh P.C., Wei J., Hardacre D., Li H. High cycle fatigue life prediction of laser additive manufactured stainless steel: A machine learning approach. Int J Fatigue 2019; 128: 105194. https://doi.org/10.1016/j.ijfatigue.2019.105194

3. Chua C.K., Leong K.F. 3D Printing and additive manufacturing: Principles and applications (with companion media pack) - fourth edition of rapid prototyping. 2014. https://doi.org/10.1142/9008

4. Tan X.P., Tan Y.J., Chow C.S.L., Tor S.B., Yeong W.Y. Metallic powder-bed based 3D printing of cellular scaffolds for orthopaedic implants: A state-of-the-art review on manufacturing, topological design, mechanical properties and biocompatibility. Materials Science and Engineering: C 2017; 76: 1328–43. https://doi.org/10.1016/j.msec.2017.02.094

5. Strickland J.D. Applications of additive manufacturing in the marine industry. Proceedings of PRADS, Denmark 2016.

6. Yap C.Y., Chua C.K., Dong Z.L., Liu Z.H., Zhang D.Q., Loh L.E., Loh L.E, Sing S.L. Review of selective laser melting: Materials and applications. Appl Phys Rev 2015; 2. https://doi.org/10.1063/1.4935926

7. Wu P., Wang J., Wang X. A critical review of the use of 3-D printing in the construction industry. Autom Constr 2016; 68: 21–31. https://doi.org/10.1016/j.autcon.2016.04.005

8. Despeisse M., Ford S. The role of additive manufacturing in improving resource efficiency and sustainability, 2015, 129–36. https://doi.org/10.1007/978-3-319-22759-7_15

9. Raj A.B., Jappes J.T.W., Khan M.A., Dillibabu V., Brintha N.C. Direct metal laser sintered (DMLS) process to develop Inconel 718 alloy for turbine engine components. Optik (Stuttg) 2020; 202: 163735. https://doi.org/10.1016/j.ijleo.2019.163735

10. Humnabad P.S., Tarun R., Das I. An overview of direct metal laser sintering (DMLS) technology for metal 3D printing. Journal of Mines, Metals and Fuels 2022; 70: 127. https://doi.org/10.18311/jmmf/2022/30681

11. Narasimharaju S.R., Liu W., Zeng W., See T.L., Scott P., Jiang X.J., Lou S. Surface texture characterization of metal selective laser melted part with varying surface inclinations. J Tribol 2021;143. https://doi.org/10.1115/1.4050455

12. Zhu Z., Lou S., Majewski C. Characterisation and correlation of areal surface texture with processing parameters and porosity of High Speed Sintered parts. Addit Manuf 2020; 36: 101402. https://doi.org/10.1016/j.addma.2020.101402

13. Gibson I., Rosen D., Stucker B. Additive manufacturing technologies. New York, NY: Springer New York; 2015. https://doi.org/10.1007/978-1-4939-2113-3

14. Bak D. Rapid prototyping or rapid production? 3D printing processes move industry towards the latter. Assembly Automation 2003; 23: 340–5. https://doi.org/10.1108/01445150310501190

15. Kim K.-S., Hwang J.-W., Lee K.-A. Effect of building direction on the mechanical anisotropy of biocompatible Co–Cr–Mo alloy manufactured by selective laser melting process. J Alloys Compd 2020; 834: 155055. https://doi.org/10.1016/j.jallcom.2020.155055

16. Srivastava A.K., Dubey A., Kumar M., Dwivedi S.P., Singh R.K., Kumar S. Measurement of form errors and comparative cost analysis for the component developed by metal printing (DMLS) and stir casting. Instrumentation Mesure Metrologie 2020; 19: 363–9. https://doi.org/10.18280/i2m.190506

17. Crisafulli D., Fintová S., Santonocito D., D'Andrea D. Microstructural characterization and mechanical behaviour of laser powder Bed Fusion stainless steel 316L. Theoretical and Applied Fracture Mechanics 2024; 131: 104343. https://doi.org/10.1016/j.tafmec.2024.104343

18. Wohler. Wohler's report 2024.

19. Nicoletto G. Anisotropic high cycle fatigue behavior of Ti–6Al–4V obtained by powder bed laser fusion. Int J Fatigue 2017; 94: 255–62. https://doi.org/10.1016/j.ijfatigue.2016.04.032

20. Avanzini A., Battini D., Gelfi M., Girelli L., Petrogalli C., Pola A., Tocci M. Investigation on fatigue strength of sand-blasted DMLS-AlSi10Mg alloy. Procedia Structural Integrity 2019; 18: 119–28. https://doi.org/10.1016/j.prostr.2019.08.146

21. Ullah R., Akmal J.S., Laakso S.V.A., Niemi E. Anisotropy of additively manufactured AlSi10Mg: threads and surface integrity. The International Journal of Advanced Manufacturing Technology 2020; 107: 3645–62. https://doi.org/10.1007/s00170-020-05243-8

22. Cordin M., Bechtold T., Pham T. Effect of fibre orientation on the mechanical properties of polypropylene–lyocell composites. Cellulose 2018; 25: 7197–210. https://doi.org/10.1007/s10570-018-2079-6

23. Zargarian A., Esfahanian M., Kadkhodapour J., Ziaei-Rad S., Zamani D. On the fatigue behavior of additive manufactured lattice structures. Theoretical and Applied Fracture Mechanics 2019; 100: 225–32. https://doi.org/10.1016/j.tafmec.2019.01.012

24. Azar A.S. Exploring the stress concentration factor in additively manufactured materials: A machine learning perspective on surface notches and subsurface defects. Theoretical and Applied Fracture Mechanics 2024; 130: 104298. https://doi.org/10.1016/j.tafmec.2024.104298

25. Miozga R., Kurek M. Effect of print orientation using DMLS method on strength of materials. MATEC Web of Conferences 2021; 338. https://doi.org/10.1051/matecconf/202133801017

26. EOS. Technical description of EOSINT M280 n.d.

27. Chadha K., Tian Y., Bocher P., Spray J.G., Aranas C. Microstructure evolution, mechanical properties and deformation behavior of an additively manufactured maraging steel. Materials 2020; 13: 2380. https://doi.org/10.3390/ma13102380

28. Sangaletti S., Aranda M.T., Távara L., García I.G. Effect of stacking direction and raster angle on the fracture properties of Onyx 3D printed components:

A mesoscale analysis. Theoretical and Applied Fracture Mechanics 2024; 129: 104228. https://doi.org/10.1016/j.tafmec.2023.104228

29. Kopec M., Gunputh U.F., Macek W., Kowalewski Z.L., Wood P. Orientation effects on the fracture behaviour of additively manufactured stainless steel 316L subjected to high cyclic fatigue. Theoretical and Applied Fracture Mechanics 2024; 130: 104287. https://doi.org/10.1016/j.tafmec.2024.104287

30. Mutua J., Nakata S., Onda T., Chen Z.-C. Optimization of selective laser melting parameters and influence of post heat treatment on microstructure and mechanical properties of maraging steel. Mater Des 2018; 139: 486–97. https://doi.org/10.1016/j.matdes.2017.11.042

31. Bai Y., Wang D., Yang Y., Wang H. Effect of heat treatment on the microstructure and mechanical properties of maraging steel by selective laser melting. Materials Science and Engineering: A 2019; 760: 105–17. https://doi.org/10.1016/j.msea.2019.05.115

32. Instron. Technical description of Instron ElecroPlus E10000 n.d.